CHINESE OPTICS LETTERS

Vol. 21, No. 2 | February 2023

# Transmissive angle-multiplexed meta-polarizer based on a multilayer metasurface

Chenxi Pu (蒲晨曦)[1], Zhuo Wang (王 卓)[1], Shulin Sun (孙树林)[2], Lei Zhou (周 磊)[1*], and Qiong He (何 琼)[1**]

[1] State Key Laboratory of Surface Physics and Department of Physics, Key Laboratory of Micro and Nano Photonic Structures (Ministry of Education), Fudan University, Shanghai 200433, China

[2] Shanghai Engineering Research Centre of Ultra-Precision Optical Manufacturing, Green Photonics and Department of Optical Science and Engineering, Fudan University, Shanghai 200433, China

*Corresponding author: phzhou@fudan.edu.cn

**Corresponding author: qionghe@fudan.edu.cn

Received May 21, 2022 | Accepted September 2, 2022 | Posted Online October 12, 2022

Metasurfaces have exhibited great capabilities to control electromagnetic waves, and many multifunctional metasurfaces were recently proposed. However, although angle-multiplexed meta-devices were successfully realized in reflection geometries, their transmission-mode counterparts are difficult to achieve due to the additional requirements. Here, we design and fabricate a transmissive angle-multiplexed meta-polarizer in the microwave regime based on a multilayer metasurface. Coupled-mode-theory analyses reveal that the device exhibits distinct angle-dependent transmissive responses under excitations with different polarizations, and such differences are further enhanced by multiple scatterings inside the device. Microwave experimental results are in good agreement with numerical simulations and theoretical analyses.

**Keywords:** metasurfaces; angular dispersion; multifunctional meta-device; polarization modulation.

**DOI:** 10.3788/COL202321.023603

## 1. Introduction

Electromagnetic (EM) integration is highly desired in modern science and technology to solve the increasing demands on memory/speed of EM devices. The key issue is to integrate different functionalities into one single device exhibiting a deep subwavelength thickness and a high working efficiency. However, multifunctional EM devices constructed with naturally existing materials are usually of bulky sizes and restricted functionalities, which are unfavorable for integration-optics applications.

Recently, metasurfaces, two-dimensional metamaterials constructed by planar meta-atoms with designable EM responses arranged in some specific global orders, have shown great capabilities to manipulate EM waves with many fascinating effects discovered[1–3], including anomalous reflection/refraction[4–6], meta-lensing[7–9], polarization conversion[10–13], meta-hologram[14–17], surface-wave manipulations[18–21], electromagnetically induced transparency[22], and many others[23–29]. Since the metasurface is flat and ultra-thin, it forms an ideal platform to realize multifunctional EM devices. Many efforts have been recently devoted to realizing metasurfaces-based multifunctional EM devices[30,31], which exhibit distinct functionalities via tuning certain parameters such as wavelength[32–34], polarization[35–37], and propagating direction[38–40] of the incident wave. Very recently, the incident angle was found to be a promising tuning parameter to realize multifunctional meta-devices[41]. However, while many angle-multiplied meta-devices are successfully realized in reflection geometries [42–45], their transmissive counterparts, which are more favorable in practical applications, are rarely found. The inherent reason is that, in designing a high-efficiency transmissive meta-device, waves on both sides of the meta-devices need to be modulated simultaneously, in contrast to the reflection-mode devices, where only the reflected waves need to be manipulated.

Here, we propose an ultra-thin transmissive multilayer metasurface in the microwave regime that can possess distinct polarization-control capabilities for impinging waves at different incident angles (see Fig. 1). Coupled-mode-theory (CMT) analyses and effective-media-theory (EMT) calculations, both in good agreement with finite-difference time-domain (FDTD) simulations on realistic structures, reveal that such angle-multiplexed functionality of our meta-system is closely related to distinct angular dispersions of Fabry–Perot (FP) resonance modes of different polarizations supported by the system. Excellent agreement among microwave experiments, numerical simulations, and theoretical analyses validates our design strategy. Our findings open up a new way to design transmissive angle-multiplexed meta-devices, which may yield many applications in practice.

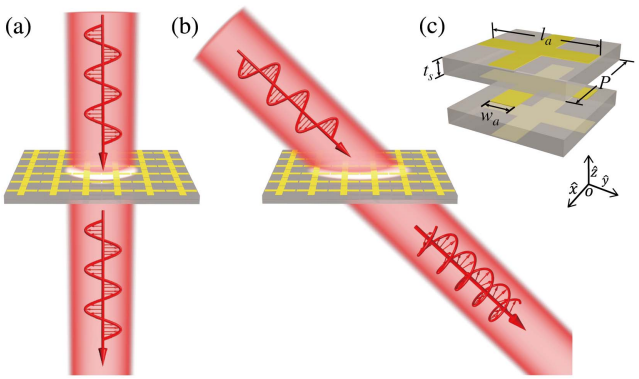


**Fig. 1.** Schematic of transmissive angle-multiplexed meta-polarizer based on multilayered isotropic metasurfaces under (a) normal and (b) oblique incidence. (c) Schematic of meta-atom design. Geometrical parameters of meta-atom: $l_a$ = 7.2 mm, $w_a$ = 1.8 mm, unit cell period $P$ = 7.5 mm, thickness of metallic film $t$ = 0.035 mm, and thickness of dielectric layer $t_s$ = 1 mm.

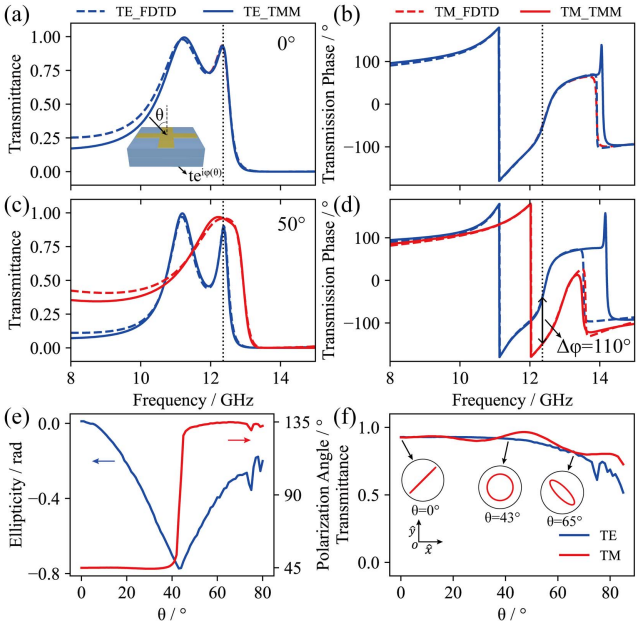


**Fig. 2.** FDTD-simulated and TMM calculated transmittance and transmission-phase spectra of our angle-multiplexed meta-polarizer for TE and TM polarized wave at the incident angle of (a), (b) 0° and (c), (d) 50°, respectively. The dashed black line indicates the working frequency of our meta-device at 12.36 GHz. (e) The variation of ellipticity and polarization angle of the transmitted wave with incident angle. (f) The variation of transmittance of TE and TM polarized waves with incident angle at 12.36 GHz. The insets of (f) depict polarization states of transmitted wave at 0°, 43°, and 65° incidence, respectively.

## 2. Results

### 2.1. Design of the angle-multiplexed meta-polarizer

In order to achieve the desired incident-angle-multiplexed polarization manipulation (see Fig. 1) efficiently, ideally the meta-system should not only exhibit high transmittance for both transverse-electric (TE, $\boldsymbol{E}\|\hat{y}$) and transverse-magnetic (TM, $\boldsymbol{H}\|\hat{y}$) polarizations under arbitrary incident angles [e.g., $|t_{\mathrm{TE}}|(\theta) = |t_{\mathrm{TM}}|(\theta) = 1$], but also exhibit pre-designed transmission-phase differences between two orthogonally polarized waves [e.g., $\Delta\varphi(\theta) = \varphi_{\mathrm{TM}}(\theta) - \varphi_{\mathrm{TE}}(\theta) \neq 0$].

To ensure high transparencies, inspired by our previous works[46,47], we choose a laterally isotropic ABA structure as the basic meta-atom to design our meta-device. As schematically shown in Fig. 1(c), our proposed meta-atom is composed by three isotropic metallic cross-shaped resonators separated by two 1-mm-thick dielectric spacers with $\varepsilon = 2.65(1 + 0.0015i)$. We first perform FDTD simulations to numerically study the transmission properties of the designed metasurface under illuminations of TE and TM polarized waves at different incident angles. Since our meta-atom exhibits four-fold rotation-invariant symmetry, it is expected that the transmission spectra for two polarizations are identical under normal incidence [Fig. 2(a)]. Meanwhile, we find in both spectra two perfect transmission windows centered at 11.2 GHz and 12.34 GHz, respectively. Figures 2(c) and 2(d) further show that our metasurface exhibits distinct EM responses for two different polarizations in terms of both transmission amplitude and phase, as the incident angle varies. Specifically, whereas two transmission peaks become slightly narrowed in the TE case (blue lines), they undergo opposite changes, and their positions are shifted to higher frequencies in the TM case (red lines), as the incident angle $\theta$ increases. Such distinct $\theta$ dependences of transmission behaviors result in considerable changes in the transmission-phase difference $\Delta\varphi(\theta)$ for two orthogonal polarizations, as $\theta$ varies [see Figs. 2(b) and 2(d)]. Choosing the working frequency as 12.36 GHz, we find that $\Delta\varphi$ can reach 110° when $\theta$ increases to 50°, where the transmittances for both polarizations are still quite high (> 89.53%). We emphasize that material losses have been taken into account in obtaining these results using our FDTD simulations. Figure 2 already implies that our device can behave as a high-efficiency incident-angle-multiplexed polarizer. As shown in Figs. 2(e) and 2(f), shining the meta-device with linearly polarized waves at different $\theta$ containing quasi-equal amplitudes of TE and TM components, we find that, whereas the transmitted wave still exhibits a linear polarization (LP) for $\theta = 0°$ due to the symmetry of the meta-atom, its polarization state changes significantly in terms of both ellipticity $\chi$ and polarization angle $\psi$, along with the increment of $\theta$. In particular, Fig. 2(f), depicting the transmittance of two polarization components (TE and TM), shows that our meta-device can change the incident LP to a nearly left-handed circular polarization (LCP) in the case of $\theta = 43°$, with an absolute working efficiency 93.37% (defined as the ratio between powers carried by the transmitted wave and the incident one) at the frequency of 12.36 GHz. In addition, more FDTD simulation results demonstrate that our meta-devices can remain the functionality of the angle-multiplexed polarization controller even with misalignment between different layers, but the performance in terms of working efficiency degrades.

### 2.2. Exploring the working mechanism of the meta-device

We now explore the working mechanism of the proposed meta-device. As discussed in Ref. [45], lateral coupling between adjacent resonators can result in changes of resonance frequency $f_0$ by varying the incident angle $\theta$, leading to the desired angular dispersions. To explore the role played by lateral couplings in our systems, we employ FDTD simulations to study the transmission spectra of our single-layer metallic structures and then employ EMT to analyze how $f_0$ varies against $\theta$. Solid lines in Figs. 3(a) and 3(b) compare the spectra of transmission amplitude and phase under two different incident angles ($\theta = 0°$ and $\theta = 50°$) for an individual meta-layer consisting of a periodical array of resonators placed on a 1-mm-thick dielectric layer [see inset of Fig. 3(a)]. Obviously, such a model well represents the top/bottom metallic layer in the designed multilayer system. We find clearly that these spectra only exhibit slight differences in terms of resonance frequencies and bandwidths, which are obviously not responsible for the significant angular dispersions discovered in our multilayer system (see Fig. 2). Note that the line shape changes under different incident angles following the Fresnel law. Quantitatively, we find that all spectra can be well modelled by an EMT model with effective permittivity of the thin metal layer described by $\varepsilon_{\text{eff}} = 1 - f_p^2/(f^2 - f_0^2 + i\gamma \cdot f)$, with $f_0 = 15.75$ GHz, $f_p = 223.3$ GHz, $\gamma = 0.017$ GHz for $\theta = 0°$ and $f_{0x} = 16.63$ GHz, $f_{px} = 232.2$ GHz, $\gamma_x = 0.028$ GHz, $f_{0y} = 14.58$ GHz, $f_{py} = 180.2$ GHz, $\gamma_y = 0.004$ GHz for $\theta = 50°$. Similar conclusions hold as we study another meta-layer consisting of a periodical array of resonators placed inside a 1-mm-thick dielectric layer, by both FDTD simulations and EMT calculations under different incident angles. Such a meta-layer well represents the middle metallic layer inside the whole device. Again, we find that $\theta$-induced changes in $f_0$ are not significant enough to explain the dramatic angular dispersions discovered in the multiplayer meta-device. To further identify the inherent reasons responsible for the strong angular dispersions, we use the transfer-matrix method (TMM) to calculate the transmission spectra of our multilayer system under two different incident angles ($\theta = 0°$ and $\theta = 50°$) in Fig. 2, with the top/bottom and middle layers replaced by their corresponding EMT models. TMM results clearly show that two new peaks appear on top of the background transmission spectra provided by the single layer [see inset of Fig. 3(a)], and such new transmission peaks exhibit much stronger angular dispersion than that in the single-layer background curve.

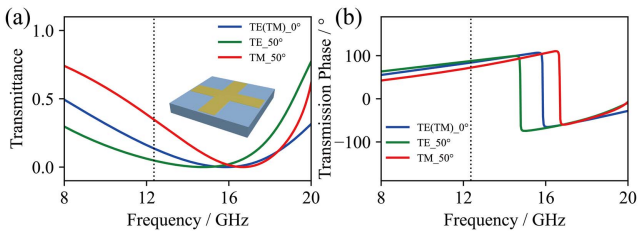


**Fig. 3.** (a) Spectra of transmittance and (b) transmission-phase for an individual meta-layer consisting of a periodical array of resonators placed on a 1-mm-thick dielectric layer [see inset of (a)] under two special incident angles (0° and 50°).

We now employ CMT to study the transmission properties of the whole system. Intuitively, two additional resonance modes are induced by multiple scatterings inside the multilayer system, responsible for the two additional transmission peaks in the transmittance spectra. Meanwhile, the symmetric system under study has both reflection and transmission channels, so that it can be well described by a two-mode two-port CMT model. Based on standard CMT analyses, we get the transmission coefficient of the whole system as

$$t = t_0 + \frac{-(r_0 + t_0)\Gamma_s^r}{-i(f - f_s) + \Gamma_s^r + \Gamma_s^i} + \frac{-\Gamma_a^r}{-i(f - f_a) + \Gamma_a^r + \Gamma_a^i}, \quad (1)$$

where $\{f_s, \Gamma_s^r, \Gamma_s^i\}$ and $\{f_a, \Gamma_a^r, \Gamma_a^i\}$ denote, respectively, the resonant frequencies, radiation damping rate, and absorption damping rate of two resonant modes in the multilayer system, and $t_0$ denotes the background transmission given by

$$t_0 = 1 + \frac{-\Gamma_0^r}{-i(f - f_0) + \Gamma_0^r + \Gamma_0^i}, \quad (2)$$

with $\{f_0, \Gamma_0^r, \Gamma_0^i\}$ describing the properties of the resonant mode in the background medium (e.g., the single-layer system). All mode parameters can be retrieved by comparing model results with corresponding simulation results on realistic structures at different incident angles. As a particular example, Figs. 4(a) and 4(b) compare the spectra of transmission amplitude and phase at $\theta = 50°$, obtained with FDTD simulations and the best-fitted CMT model. Good agreement between these two spectra is noted.

Figures 4(c) and 4(d) plot the retrieved model parameters $f_s$, $f_a$, $\Gamma_s^r$, and $\Gamma_a^r$ at different incident angles for TE and TM polarizations, respectively. As shown in Fig. 2, two resonant modes under different polarizations do exhibit distinct or even opposite angle-dependent properties, which also well explain the strong angular dispersions in the transmission spectra. Figures 4(e) and 4(f) depict the distributions of $\text{Re}(E_y)/|E_0|$ on the center $y$–$z$ plane inside a meta-atom for two resonance modes at normal incidence, where $|E_0|$ represents the $E$-field of the incident wave. We find that the mode at 11.14 GHz is exactly an antisymmetric mode, while that at 12.43 GHz is clearly a symmetric mode, generated by coupling the FP modes supported by two cavities formed by adjacent metallic layers.

The physics underlying the intriguing angular dispersions presented in Figs. 4(c) and 4(d) is thus clear. Since such FP-like resonances are induced by multiple scatterings inside the multilayer system, their optical characteristics (e.g., resonance frequency and radiation damping) are closely related to the reflection properties of the mirrors (i.e., the metallic layers) forming the cavities. Figures 4(g) and 4(h) depict how the reflectance of the top metallic layer varies against incident angle and frequency for TE and TM polarizations, respectively. Clearly, we find that $R_{\text{TE}}$ and $R_{\text{TM}}$ exhibit opposite dependences on incident

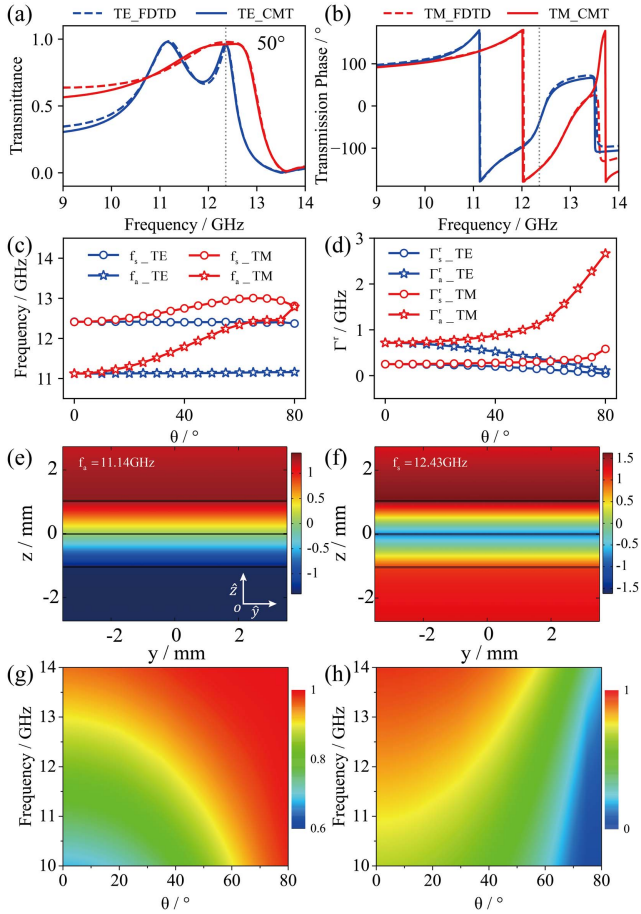


**Fig. 4.** FDTD-simulated and CMT calculated spectra of (a) transmittance and (b) transmission-phase of our meta-design at the incident angle of 50°. The variation of (c) resonant frequency and (d) radiation damping rate of two resonant modes with incident angle. The distribution of Re($E_y$)/$|E_0|$ on the center *y*–*z* plane inside a meta-atom of (e) antisymmetrical and (f) symmetrical modes retrieved by CMT under normal illumination with TE-polarized plane wave, with $|E_0|$ being the electric field intensity of the input wave. The atom is placed parallel to the *xoy* plane, and the patterns of Re($E_x$)/$|E_0|$ for the TM-polarized plane wave are identical. Distribution of reflectance of individual top meta-layer [see inset of Fig. 3(a)] as a function of incident angle and frequency under the illumination of (g) TE and (h) TM polarized waves, respectively.

angle $\theta$. Taking the working frequency 12.36 GHz as an example, whereas $R_{TE}$ increases from 0.86 to 0.95 as $\theta$ changes from 0° to 50°, $R_{TM}$ decreases from 0.86 to 0.65. Such opposite angle dependences on Fresnel coefficients are ultimately caused by opposite angle dependences on the effective impedance of a dielectric surface for two different polarizations. Therefore, it is natural to see that increasing $\theta$ can increase (decrease) the quality ($Q$) factor of those FP modes in the TE (TM) case (see Fig. 2) due to enhanced (diminished) reflectance of the metallic mirrors forming the cavity. Meanwhile, variations of reflectance of the middle metallic layer can effectively change the coupling between two cavity modes, which together with the influence of variations of other interfacial Fresnel coefficients leads to shifts of resonance frequencies. These effects collectively result in dramatically different angle-dependent transmission behaviors for TE and TM polarizations, as revealed in Fig. 2. In fact, it is the different evolutions of the two collective modes for TE and TM polarization that lead to different line shapes of the transmittance and transmission-phase spectrum at the same incident angle, offering the possibility to realize angle-multiplexed functional meta-devices.

## 2.3. Experimental demonstrations and design optimizations

We now perform microwave experiments to verify our design. We fabricate out the designed meta-device in a size of 46.5 cm × 49.5 cm [see Fig. 5(a)] and measure its transmission spectra using a vector network analyzer (Agilent E8362C PNA) under different incident angles. A pinhole system is adopted in our measurements to suppress the finite-size effect. It is worth noting that the fabricated sample possesses an additional adhesive layer to stick different meta-layers together [see Fig. 5(b)], which breaks the inversion symmetry and adds more losses to the meta-device. The side effects contributed by the adhesive layer deviate the positions of transmission peaks in a realistic case from the expected ones in design and deteriorate the performances of the device in terms of efficiency and ellipticity. Figures 5(c) and 5(d) plot the measured transmittance for different polarizations and $\Delta\varphi$ as functions of $\theta$ at the working frequency of 11.7 GHz. Taking the adhesive layer into our FDTD simulations, we find a good agreement between experiments and full-wave simulations in terms of both transmittance

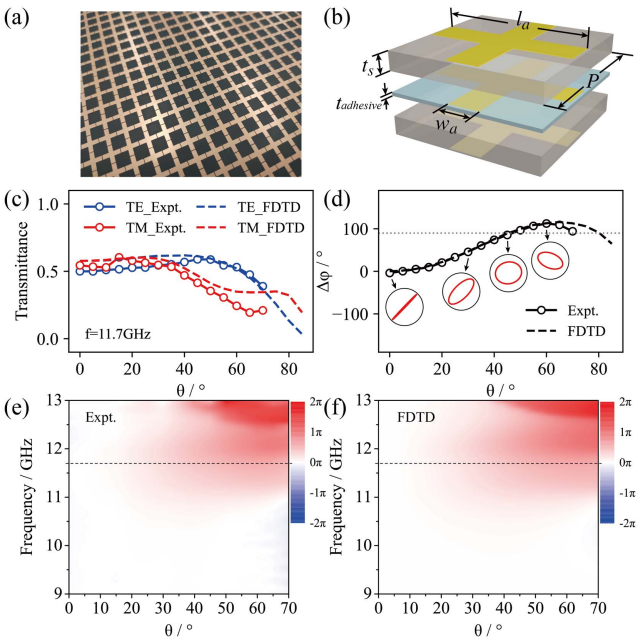


**Fig. 5.** (a) Picture of fabricated sample. (b) Schematic of realistic meta-atom with $\varepsilon_{adhesive}$ =4.2 (1 + 0.025*i*), $t_{adhesive}$ = 0.18 mm, $t_s$ = 0.93 mm, $w_a$ = 1.8 mm. Measured and FDTD-simulated (c) transmittance and (d) $\Delta\varphi$ for TE and TM polarizations as a function of the incident angle at the working frequency of 11.7 GHz. (e) Measured and (f) simulated *f*-$\theta$ phase diagram of $\Delta\varphi$.

and $\Delta\varphi$ at different frequencies and incident angles $\theta$, as shown in Figs. 5(c)–5(f). In particular, we find desirable transmission-phase differences $\Delta\varphi$ in a wide region of the $f$-$\theta$ phase diagram. Taking the case of $\{f = 11.7\,\text{GHz}, \theta = 45°\}$ as an explicit example, we find that both measured and simulated $\Delta\varphi$ can reach 90°, while the measured transmittance reaches 58.9% (61.27%) and 41.48% (46.88%) for TE and TM polarizations, respectively. Therefore, our meta-device can convert a linearly polarized incident wave with equal amplitudes of TE and TM components into a (nearly) circularly polarized wave with measured (simulated) polarization ellipticity of −0.6897 (−0.7182) and absolute working efficiency of 49.72% (53.84%) at the incident angle of 45°. Adjusting the weights of TE and TM components inside the incident beam, we can easily modulate the polarization ellipticity of the transmitted wave.

We finally discuss how to improve the performance of our meta-device based on FDTD simulations. As discussed above, the adhesive layer breaks the inversion symmetry and increases the absorption, which is responsible for transmittance reduction discovered in experiments. Keeping the adhesive layer inside the sample, we can optimize the geometric structures of the resonators to minimize their influences. Figure 6(a) depicts the FDTD-simulated normal-incidence transmittance spectra of our realistic sample but with the width of metallic bar $w_a$ taking different values. Simulation results show that the transmittance at the working frequency of 11.7 GHz can be improved from 0.58 to 0.7 as $w_a$ takes a value of 2.3 mm, since varying the width of the metallic bar in a resonator can change not only the $Q$ factor but also the coupling of two cavity modes supported by adjacent metallic layers, which affects the transmittance eventually. On the other hand, to remedy the symmetry-breaking issue in the realized sample, we propose a new structure in which the middle metallic layer is now buried in the middle of the adhesive layer. Figure 6(b) compares the simulated transmission spectra of the symmetric and original structures with $w_a$ = 2.3 mm. One can readily find that the transmittance can be further improved from 0.7 to 0.81 via adopting the proposed symmetric configuration. The underlying physics is that perfect transparency in such an ABA structure is closely related to the inversion symmetry possessed by the system.

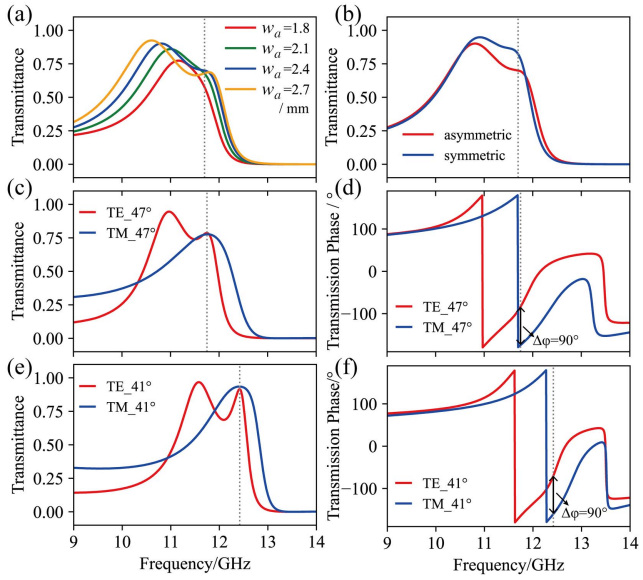


**Fig. 6.** Performance optimization of our meta-polarizer performance. (a) FDTD-simulated transmittance spectra for the meta-polarizer with different $w_a$ under normal incidence. (b) FDTD-simulated transmittance spectra for the meta-polarizer with different degrees of symmetry under normal incidence with $w_a$ = 2.3 mm. FDTD-simulated (c) transmittance and (d) transmission-phase spectra for the optimized meta-polarizer with $w_a$ = 2.3 mm in a symmetric configuration at the incident angle of 47°. The other optimized geometrical parameters are consistent with experiment. FDTD-simulated (e) transmittance and (f) transmission-phase spectra for the optimized meta-polarizer without the adhesive layer at the incident angle of 41°. The optimized cross width $w_a$ = 1.5 mm.

We now numerically examine the performance of the optimized metasurface (i.e., with $w_a$ = 2.3 mm and in symmetric configuration as well). Figures 6(c) and 6(d) show the simulated spectra of transmittance and transmission-phase for both TE and TM polarizations at $\theta = 47°$. At the working frequency of 11.75 GHz, we find that the working efficiency of our meta-device can be improved to 78.13% with a polarization ellipticity of the transmitted being −0.7797. Finally, suppose we do not need to use the lossy adhesive layer; then the working efficiency of our meta-device can be further enhanced to 92.54% at $\theta = 41°$ and 91.95% at normal incidence, as shown in Figs. 6(e) and 6(f), where the simulated spectra of transmittance and transmission-phase for such a device are depicted. It should be noted that now the working frequency has been changed to 12.42 GHz accordingly. In addition to the previously mentioned optimization methods, we can increase the transmissive phase difference between TE and TM modes by adding additional dielectric and metallic resonator layers and enlarging the working bandwidth by reducing the $Q$ factor or/and coupling of cavity modes by further optimizing the geometrical parameters.

## 3. Conclusions

In summary, we propose an angle-multiplexed meta-polarizer in the transmission mode based on a multilayer metasurface and experimentally realize it in the microwave regime. CMT analyses, supported by full-wave simulations, reveal that such angle-multiplexed polarization manipulations are dictated by distinct angular dispersions of two vertical resonances inside the system, which result in distinct angle-dependent transmissive responses for TE and TM polarized waves. Reasonable agreement among experiments, simulation, and theoretical results justifies our design strategy, and meta-devices with better performances can be realized through reducing material losses and keeping the inversion symmetries in fabrications. Our findings provide a transmissive platform to realize angle-multiplexed meta-devices, which can stimulate many interesting applications in optoelectronics.

## Acknowledgement

This work was supported by the National Natural Science Foundation of China (Nos. 11734007, 62192771, and 91850101), National Key Research and Development Program of China (Nos. 2017YFA0303504 and 2020YFA0710100), and Natural Science Foundation of Shanghai (No. 20JC1414601).

## References

1. N. Yu and F. Capasso, "Flat optics with designer metasurfaces," Nat. Mater. **13**, 139 (2014).
2. F. Ding, A. Pors, and S. I. Bozhevolnyi, "Gradient metasurfaces: a review of fundamentals and applications," Rep. Prog. Phys. **81**, 026401 (2018).
3. S. Sun, Q. He, J. Hao, S. Xiao, and L. Zhou, "Electromagnetic metasurfaces: physics and applications," Adv. Opt. Photonics **11**, 380 (2019).
4. N. F. Yu, P. Genevet, M. A. Kats, F. Aieta, J. P. Tetienne, F. Capasso, and Z. Gaburro, "Light propagation with phase discontinuities: generalized laws of reflection and refraction," Science **334**, 333 (2011).
5. X. Ni, N. K. Emani, A. V. Kildishev, A. Boltasseva, and V. M. Shalaev, "Broadband light bending with plasmonic nanoantennas," Science **335**, 427 (2012).
6. S. Sun, Q. He, S. Xiao, Q. Xu, X. Li, and L. Zhou, "Gradient-index meta-surfaces as a bridge linking propagating waves and surface waves," Nat. Mater. **11**, 426 (2012).
7. X. Li, S. Y. Xiao, B. G. Cai, Q. He, T. J. Cui, and L. Zhou, "Flat metasurfaces to focus electromagnetic waves in reflection geometry," Opt. Lett. **37**, 4940 (2012).
8. M. Khorasaninejad, W. T. Chen, R. C. Devlin, J. Oh, A. Y. Zhu, and F. Capasso, "Metalenses at visible wavelengths: diffraction-limited focusing and subwavelength resolution imaging," Science **352**, 1190 (2016).
9. R. J. Lin, V. C. Su, S. Wang, M. K. Chen, T. L. Chung, Y. H. Chen, H. Y. Kuo, J. W. Chen, J. Chen, Y. T. Huang, J. H. Wang, C. H. Chu, P. C. Wu, T. Li, Z. Wang, S. Zhu, and D. P. Tsai, "Achromatic metalens array for full-colour light-field imaging," Nat. Nanotechnol. **14**, 227 (2019).
10. J. Hao, Y. Yuan, L. Ran, T. Jiang, J. A. Kong, C. T. Chan, and L. Zhou, "Manipulating electromagnetic wave polarizations by anisotropic metamaterials," Phys. Rev. Lett. **99**, 063908 (2007).
11. W. J. Sun, Q. O. He, J. M. Hao, and L. Zhou, "A transparent metamaterial to manipulate electromagnetic wave polarizations," Opt. Lett. **36**, 927 (2011).
12. S. Jiang, X. Xiong, Y. Hu, Y. Hu, G. Ma, R. Peng, C. Sun, and M. Wang, "Controlling the polarization state of light with a dispersion-free metastructure," Phys. Rev. X **4**, 021026 (2014).
13. J. P. B. Mueller, N. A. Rubin, R. C. Devlin, B. Groever, and F. Capasso, "Metasurface polarization optics: independent phase control of arbitrary orthogonal states of polarization," Phys. Rev. Lett. **118**, 113901 (2017).
14. G. Zheng, H. Muhlenbernd, M. Kenney, G. Li, T. Zentgraf, and S. Zhang, "Metasurface holograms reaching 80% efficiency," Nat. Nanotechnol. **10**, 308 (2015).
15. L. Wang, S. Kruk, H. Tang, T. Li, I. Kravchenko, D. N. Neshev, and Y. S. Kivshar, "Grayscale transparent metasurface holograms," Optica **3**, 1504 (2016).
16. G. Zheng, N. Zhou, L. Deng, G. Li, J. Tao, and Z. Li, "Full-space metasurface holograms in the visible range," Opt. Express **29**, 2920 (2021).
17. L. Huang, S. Zhang, and T. Zentgraf, "Metasurface holography: from fundamentals to applications," Nanophotonics **7**, 1169 (2018).
18. D. Wang, F. Liu, T. Liu, S. Sun, Q. He, and L. Zhou, "Efficient generation of complex vectorial optical fields with metasurfaces," Light Sci. Appl. **10**, 67 (2021).
19. W. Sun, Q. He, S. Sun, and L. Zhou, "High-efficiency surface plasmon meta-couplers: concept and microwave-regime realizations," Light Sci. Appl. **5**, e16003 (2016).
20. F. Ding, R. Deshpande, and S. I. Bozhevolnyi, "Bifunctional gap-plasmon metasurfaces for visible light: polarization-controlled unidirectional surface plasmon excitation and beam steering at normal incidence," Light Sci. Appl. **7**, 17178 (2018).
21. L. Huang, X. Chen, B. Bai, Q. Tan, G. Jin, T. Zentgraf, and S. Zhang, "Helicity dependent directional surface plasmon polariton excitation using a metasurface with interfacial phase discontinuity," Light Sci. Appl. **2**, e70 (2013).
22. K. Liu, X. Chen, M. Lian, J. Jia, Y. Su, H. Ren, S. Zhang, Y. Xu, J. Chen, Z. Tian, and T. Cao, "Nonvolatile reconfigurable electromagnetically induced transparency with terahertz chalcogenide metasurfaces," Laser Photonics Rev. **16**, 2100393 (2022).
23. W. Liu, Z. Li, H. Cheng, C. Tang, J. Li, S. Zhang, S. Chen, and J. Tian, "Metasurface enabled wide-angle Fourier lens," Adv. Mater. **30**, 1706368 (2018).
24. G. Y. Lee, J. Y. Hong, S. Hwang, S. Moon, H. Kang, S. Jeon, H. Kim, J. H. Jeong, and B. Lee, "Metasurface eyepiece for augmented reality," Nat. Commun. **9**, 4562 (2018).
25. A. H. Dorrah, N. A. Rubin, A. Zaidi, M. Tamagnone, and F. Capasso, "Metasurface optics for on-demand polarization transformations along the optical path," Nat. Photonics **15**, 287 (2021).
26. R. Yalavarthi, O. Yesilyurt, O. Henrotte, Š. Kment, V. M. Shalaev, A. Boltasseva, and A. Naldoni, "Multimetallic metasurfaces for enhanced electrocatalytic oxidations in direct alcohol fuel cells," Laser Photonics Rev. **16**, 2200137 (2022).
27. Y. Wu, Y. Wang, W. Yang, Q. Song, Q. Chen, G. Qu, J. Han, and S. Xiao, "Self-cleaning titanium dioxide metasurfaces with UV irradiation," Laser Photonics Rev. **15**, 2000330 (2020).
28. J. Ma, F. Xie, W. Chen, J. Chen, W. Wu, W. Liu, Y. Chen, W. Cai, M. Ren, and J. Xu, "Nonlinear lithium niobate metasurfaces for second harmonic generation," Laser Photonics Rev. **15**, 2000521 (2021).
29. Z. Hao, W. Liu, Z. Li, Z. Li, G. Geng, Y. Wang, H. Cheng, H. Ahmed, X. Chen, J. Li, J. Tian, and S. Chen, "Full complex-amplitude modulation of second harmonic generation with nonlinear metasurfaces," Laser Photonics Rev. **15**, 2100207 (2021).
30. B. Xiong, L. Deng, R. Peng, and Y. Liu, "Controlling the degrees of freedom in metasurface designs for multi-functional optical devices," Nanoscale Adv. **1**, 3786 (2019).
31. Z. Li, S. Yu, and G. Zheng, "Advances in exploiting the degrees of freedom in nanostructured metasurface design: from 1 to 3 to more," Nanophotonics **9**, 3699 (2020).
32. R. Xie, M. Xin, S. Chen, D. Zhang, X. Wang, G. Zhai, J. Gao, S. An, B. Zheng, H. Zhang, and J. Ding, "Frequency-multiplexed complex-amplitude meta-devices based on bispectral 2-bit coding meta-atoms," Adv. Opt. Mater. **8**, 2000919 (2020).
33. H. Lu, B. Zheng, T. Cai, C. Qian, Y. Yang, Z. Wang, and H. Chen, "Frequency-controlled focusing using achromatic metasurface," Adv. Opt. Mater. **9**, 2001311 (2020).
34. J. Sisler, W. T. Chen, A. Y. Zhu, and F. Capasso, "Controlling dispersion in multifunctional metasurfaces," APL Photonics **5**, 056107 (2020).
35. T. Cai, G. M. Wang, S. W. Tang, H. X. Xu, J. W. Duan, H. J. Guo, F. X. Guan, S. L. Sun, Q. He, and L. Zhou, "High-efficiency and full-space manipulation of electromagnetic wave fronts with metasurfaces," Phys. Rev. Appl. **8**, 034033 (2017).
36. Z. L. Deng, J. Deng, X. Zhuang, S. Wang, T. Shi, G. P. Wang, Y. Wang, J. Xu, Y. Cao, X. Wang, X. Cheng, G. Li, and X. Li, "Facile metagrating holograms with broadband and extreme angle tolerance," Light Sci. Appl. **7**, 78 (2018).
37. T. Yan, Q. Ma, S. Sun, Q. Xiao, I. Shahid, X. Gao, and T. J. Cui, "Polarization multiplexing hologram realized by anisotropic digital metasurface," Adv. Theory Simul. **4**, 2100046 (2021).
38. C. Zhang, G. Wang, H. X. Xu, X. Zhang, and H. P. Li, "Helicity-dependent multifunctional metasurfaces for full-space wave control," Adv. Opt. Mater. **8**, 1901719 (2020).
39. L. Zhang, R. Y. Wu, G. D. Bai, H. T. Wu, Q. Ma, X. Q. Chen, and T. J. Cui, "Transmission-reflection-integrated multifunctional coding metasurface for full-space controls of electromagnetic waves," Adv. Funct. Mater. **28**, 1802205 (2018).
40. K. Chen, G. Ding, G. Hu, Z. Jin, J. Zhao, Y. Feng, T. Jiang, A. Alu, and C. W. Qiu, "Directional Janus metasurface," Adv. Mater. **32**, 1906352 (2020).
41. H.-H. Hsiao, C. H. Chu, and D. P. Tsai, "Fundamentals and applications of metasurfaces," Small Methods **1**, 1600064 (2017).

42. S. M. Kamali, E. Arbabi, A. Arbabi, Y. Horie, M. Faraji-Dana, and A. Faraon, "Angle-multiplexed metasurfaces: encoding independent wavefronts in a single metasurface under different illumination angles," Phys. Rev. X **7**, 041056 (2017).
43. A. Leitis, A. Tittl, M. K. Liu, B. H. Lee, M. B. Gu, Y. S. Kivshar, and H. Altug, "Angle-multiplexed all-dielectric metasurfaces for broadband molecular fingerprint retrieval," Sci. Adv. **5**, eaaw2871 (2019).
44. X. Zhang, Q. Li, F. Liu, M. Qiu, S. Sun, Q. He, and L. Zhou, "Controlling angular dispersions in optical metasurfaces," Light Sci. Appl. **9**, 76 (2020).
45. M. Qiu, M. Jia, S. Ma, S. Sun, Q. He, and L. Zhou, "Angular dispersions in terahertz metasurfaces: physics and applications," Phys. Rev. Appl. **9**, 054050 (2018).
46. L. Zhou, W. Wen, C. T. Chan, and P. Sheng, "Electromagnetic-wave tunneling through negative-permittivity media with high magnetic fields," Phys. Rev. Lett. **94**, 243905 (2005).
47. W. Luo, S. Sun, H.-X. Xu, Q. He, and L. Zhou, "Transmissive ultrathin Pancharatnam-Berry metasurfaces with nearly 100% efficiency," Phys. Rev. Appl. **7**, 044033 (2017).